Superelement modelling of elastic metamaterials: Complex dispersive properties of three-dimensional structured beams and plates

Journal of Sound and Vibration 484 (2020) 115499

Contents lists available at ScienceDirect

Journal of Sound and Vibration

journal homepage: www.elsevier.com/locate/jsvi

Superelement modelling of elastic metamaterials: Complex dispersive properties of three-dimensional structured beams and plates

Domenico Tallarico [a,*], Gwenael Hannema [a], Marco Miniaci [b], Andrea Bergamini [a], Armin Zemp [a], Bart Van Damme [a]

[a] Laboratory for Acoustics/ Noise Control, Swiss Federal Laboratories for Materials Science and Technology (EMPA), Überlandstrasse 129, 8600, Dübendorf, Switzerland
[b] CNRS, Centrale Lille, ISEN, Univ. Lille, Univ. Valenciennes, UMR 8520 - IEMN, F-59000, Lille, France

ARTICLE INFO

Article history:
Received 13 January 2020
Revised 25 May 2020
Accepted 3 June 2020
Available online 10 June 2020
Handling Editor: Erasmo Carrera

Keywords:
Elastic metamaterials
Numerical reduction
Dispersive properties

ABSTRACT

In this article, we offer a fast calculation method for the dispersive properties of three-dimensional micro-structured solids with one-dimensional and two-dimensional translation symmetry. We review mathematical methods to obtain the complex dispersion diagram for such structures (*i.e.* the Bloch vector as a function of frequency). This can be done by solving a Bloch-Floquet eigenvalue problem which is non-linear in the Bloch vector. Such a problem inevitably calls for reduction methods as the required number of degrees of freedom of the unit cell increases. Therefore, an asymptotic-in-frequency technique is implemented in order to approximate the dynamic stiffness matrix of the unit cell. This is done by identifying and retaining the most significant nodal degrees-of-freedom, which are used to generate a unit cell "superelement". The accuracy of the Bloch vectors and corresponding eigenvectors associated with the reduced non-linear eigenvalue problem is demonstrated by direct comparison to full-size computations and shows excellent agreement combined with considerable computing time reduction and controllable limitations.

1. Introduction

A considerable research effort is currently devoted to the study of engineered elastic materials with periodically repeating microstructure. The interest in such materials - also referred to as elastic metamaterials - arises mainly from unusual and fascinating phenomena, such as dynamic anisotropy, tunable group velocity and forbidden frequency regions (band gaps). Those dispersive properties often result in useful applications such as tunable band gaps for elastic waves [1,2], focusing via negative refraction [3,4], unidirectional wave propagation in active elastic media [5,6], and topological protection of edge modes in passive micro-structured plates [7]. Although the aforementioned phenomena are all observable in finite-size structures, they can be predicted by the analysis of the dispersive properties of their periodic counterparts. From a mathematical point of view, the calculation of the dispersion diagrams for such materials traces back to the solution of special eigenvalue problems posed on the spatial period of the structure (the unit cell) whose boundaries satisfy so-called Bloch-Floquet boundary conditions [8].

* Corresponding author.
E-mail address: domenico.tallarico@empa.ch (D. Tallarico).

https://doi.org/10.1016/j.jsv.2020.115499

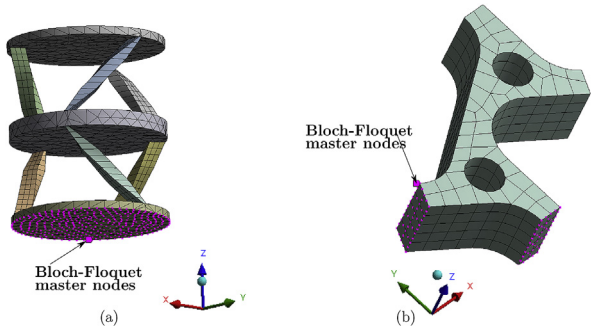

Fig. 1. Unit cell geometries with quadratic mesh overlaid. Panel (a) is the unit cell for a structured $z-$periodic beam and panel (b) is the unit cell of a triangular lattice in the (x, y) plane. The purple dots represent the nodes corresponding to the full Bloch-Floquet master faces. Geometry and material parameters are the same as those used in Ref. [7,43], respectively. (For interpretation of the references to color in this figure legend, the reader is referred to the Web version of this article.)

Few design and computational approaches currently go beyond Bloch-Floquet dispersive properties. Some examples are direct lattice transformation techniques [9], transformation elastodynamics [10] (e.g. Ref. [11] for in-plane wave formulation [12], for a flexural wave formulation) and transformation acoustics [13]. For weakly non-linear periodic structures, dispersion relations for elastic waves have been obtained using multiple-harmonic expansion techniques (e.g. Ref. [14] for periodic Euler-Bernoulli beams and [15] Lamb waves in plates). Other examples inherently transcending the linear Bloch-Floquet framework are geometrically non-linear structured media, e.g. Ref. [16] for recent modelling advances [17], for solitons propagation in prestressed unit cells [18], for "elastic diodes" based on bi-stable elements [19,20], for models of the dynamic response of elastic structures with localised non-linearities.

Discretised one-dimensional problems in structural dynamics were considered in Ref. [21] focusing on unit cells of 1D periodic continuous systems using a finite number of displacement coordinates. In this framework, often referred to as "indirect method", a real spectral parameter k is fixed and the unknown Bloch frequencies are computed solving a quadratic or linear eigenvalue problem, according to whether damping is present or negligible, respectively. The value k identifies here either the one-dimensional (1D) Bloch wave number or the modulus of the two-dimensional (2D) Bloch vector, according to whether 1D or 2D translational symmetries are considered. The work [21] was later extended in Ref. [22], where the main contribution was to incorporate the unit cell's boundary conditions within a functional used in a variational principle. This method allows calculating the complex propagation constant for a Bloch wave of given angular frequency, and is usually referred to as "direct method".

The pioneering works [21,22] provided the background for the subsequent introduction of the so called wave/finite element method, established by Mace and Manconi [23]. The method relies on the following steps, to be performed at each frequency:

- elimination of internal degrees-of-freedom (dofs) via dynamic condensation;
- solution of a non-linear eigenvalue problem for k defined over master Bloch-Floquet boundary nodes (see Fig. 1).

The direct Bloch eigenvalue problem for the modulus of the Bloch vector k is transcendental, but it can be reduced to a polynomial form for appropriately chosen propagation angles. More recently the direct method has been used to design locally resonant metamaterials [24,25] and 2D phononic crystals [26]. In the context of Bloch-Floquet direct methods, Collet et al. [27] incorporated the Bloch-Floquet boundary conditions into a new set of bulk partial differential equations (PDEs) satisfying continuity boundary conditions, and later solved using standard finite-element techniques. The method has been extended by Wang et al. [28] to model in-plane wave dispersion and transmission in linear viscoelastic plane-strain structures. In the framework of direct methods, Mazzotti et al. [29] proposed a variational fluid-structure interaction model to solve the dispersion problem in an acoustic half-space loading a phononic crystal slab and accounting for leaky Bloch modes into the acoustic domain.

Bloch-Floquet eigenvalue problems are gradually permeating structural engineering practices for the design of meta-structures. As a motivation example, one may want to know how many unit cells within an assembly are needed in order to obtain a desired wave attenuation in a given frequency range within the band gap of the periodic counterpart. The answer is readily provided by the direct Bloch-Floquet eigenvalue problem $k(\omega)$. If an attenuation α is sought, the decaying length can be obtained as

$$\lambda = -\ln(\alpha)/\mathrm{Im}(k). \tag{1}$$

Another motivation for formulating the problem in terms of Bloch vectors rather than frequency, comes from boundary-value problems in dynamics involving scattering of waves by elastic gratings or microstructured slabs (see e.g. Ref. [30,31]). In fact, such problems rely on the conservation of the parallel component of the incident wave vector to an interface (Snell's law [32]). If the scattering half-space or slab is microstructured, then the wave vector is exactly the Bloch vector, to be computed solving a direct Bloch-Floquet auxiliary problem. In this context, Laude et al. [33] have adapted the plane-wave expansion (PWE) method to accommodate complex wave-vectors resulting from the dispersion diagram of unit cells comprising both scalar (out-of-plane) and 2D (in-plane) elastic fields.

A considerable downside of the direct method is the fact that polynomial eigenvalue problems of high degree are time consuming to solve. This is further complicated by the fact that the dynamic stiffness matrix (DSM) is often very large for realistic, complex 3D unit cells. Several methods already exist in order to approximate the finite-element (FE) DSM of unit cells by a lower order problem. Those can be grouped in *spatial reduction techniques*, where the projection of the dynamic stiffness matrix onto a set of spatial nodal dofs is performed [34]; *eigenmode-based* techniques, where the dynamic stiffness matrix is approximated by retaining a reduced set of free [35] or fixed [36] eigenmodes for the unit cell, together with boundary nodes; and *asymptotic* techniques, where the dynamic stiffness matrix is expanded in a power series of the frequency (see Ref. [37] for the expansion up to the first non-trivial order). Combinations of the aforementioned methods with application into vibro-acoustics are also possible [38].

The aforementioned broad reduction categories display advantages and disadvantages according to the computational purposes they are used for. Spatial reduction techniques perform very well if the local response is sought but, due to their local nature, are not suitable for dispersion calculation. Eigenmode-based techniques are typically very accurate both for eigenvalue and dynamic response computations of assemblies of structural components. However, they rely on the retention of the full set of boundary nodes, which makes them ineffective for the solution polynomial eigenvalue problems defined over such set (second computational step for the direct Bloch-Floquet method). In this article we offer a way to ease the numerical demand of direct non-linear Bloch-Floquet eigenvalue problems using existing asymptotic technique for the approximation of the DSM, *i.e.* Guyan superelements [37]. This reduction method is often used for linear eigenvalue problems, and it is well known to display poor accuracy above a certain frequency threshold, especially if the retained nodes after the expansion are not appropriately chosen [39]. Here, both reduction and accuracy of the method in a given frequency range are addressed for several 3D unit cells with 1D or 2D translation symmetry. First, an algorithmic choice of the retained nodal dofs is presented. The accuracy of the Guyan superelement is then demonstrated for eigenvalue problems of the unit cell with free boundary conditions. The reduced DSM is subsequently used in the formulation and solution of direct Bloch-Floquet problems. In this context, the recent articles [40–42] address the Craig-Bampton reduction of the wave finite element dispersion for locally resonant metamaterials. In addition, in Ref. [41,42], the authors give useful insight on local frequency response functions for assemblies of unit cells. However, the authors focused their analysis on slender unit cells, limiting their attention to the effective elimination of internal nodal dofs which does not reduce the (inherently small) dimension of the Bloch-Floquet non-linear eigenvalue problem. In the current paper 3D non-slender unit cells are considered, arranged to form a micro-structured beam [43] or a micro-structured plate [7]. The reduction studied here aims at reducing not only the internal, but also the boundary nodes. The obtained reduced direct Bloch-Floquet eigenvalue problem for the unit cells leads to a good qualitative comparison with the full model and a considerable time saving. Importantly, dispersive phenomena such as band gaps and high-frequency double Dirac cones are captured by the reduced model. We opted for an asymptotic reduction method rather than an eigenmode-based reduction, because the former allows to assess the accuracy against the percentage of eliminated both internal and boundary nodal dofs, whereas the latter relies on the full set of boundary nodes, resulting in the full polynomial eigenvalue problem.

The manuscript is organised as follows. In section 2 we review the steps needed in order to perform a direct Bloch-Floquet computation for 1D and 2D periodic structures. The structure with 2D translational symmetry is a triangular lattice for which, in section 2.3, we specify how to capture the direct Bloch-Floquet dispersion along the edges of the first Brillouin zone without computing the dispersion at every angle. In section 3, the reduction of the unit cell is formally performed over a set of "retained" nodal dofs. The accuracy of the proposed algorithmic choice is tested over free eigenvalue problems of the unit cell, for different percentages of nodal dofs eliminations. In section 4, we present the complex dispersive properties of the selected structures, comparing the full model to the reduced model. The accuracy and the reduction of computational time are discussed. Finally, in section 5 we provide our conclusions, including limitations of the proposed method.

2. The direct Bloch-Floquet eigenvalue problem

For a linear elastic body, the FE discretisation of the PDEs of elasticity, leads to the algebraic governing equations for the time-harmonic nodal dofs $\boldsymbol{U}$

$$\left(\boldsymbol{\mathcal{K}} - \omega^2 \boldsymbol{\mathcal{M}}\right) \boldsymbol{U} = \boldsymbol{f}. \tag{2}$$

The vectors are $\boldsymbol{U}, \boldsymbol{f} \in \mathbb{C}^N$, where $\boldsymbol{f}$ is the external body force acting on the nodal coordinates, $\boldsymbol{\mathcal{K}}, \boldsymbol{\mathcal{M}} \in \mathbb{R}^{N \times N}$ are the symmetric stiffness and mass matrices, $N = 3n \gg 1$ is a natural number representing the total number of FE dofs, n being the number of nodes in the FE discretisation, and ω is the angular frequency. The matrix $\boldsymbol{\mathcal{K}} - \omega^2 \boldsymbol{\mathcal{M}}$ is the full dynamic stiffness matrix, defined over the full set of nodal dofs $\boldsymbol{U}$.

2.1. Periodic boundary conditions

We consider a periodic assembly of unit cells, in the absence of external forces. The governing system of equations for the time harmonic nodal displacement in Eq. (2) can be segmented in a convenient way by assuming that

$$\boldsymbol{f} = \begin{pmatrix} \boldsymbol{f}_b \\ \boldsymbol{0} \end{pmatrix}, \tag{3}$$

where $\boldsymbol{f}_b$ are boundary tractions resulting from the interaction of a unit cell (e.g. those in Fig. 1) with the nearest neighbours defined over boundary nodal dofs b. Accordingly, Eq. (2) becomes

$$\begin{pmatrix} \boldsymbol{\mathcal{D}}_{bb}(\omega) & \boldsymbol{\mathcal{D}}_{bi}(\omega) \\ \boldsymbol{\mathcal{D}}_{ib}(\omega) & \boldsymbol{\mathcal{D}}_{ii}(\omega) \end{pmatrix} \begin{pmatrix} \boldsymbol{\phi}_b \\ \boldsymbol{\phi}_i \end{pmatrix} = \begin{pmatrix} \boldsymbol{f}_b \\ \boldsymbol{0} \end{pmatrix}, \tag{4}$$

where $\boldsymbol{\mathcal{D}}_{\ell j}(\omega) = \boldsymbol{\mathcal{K}}_{\ell j} - \omega^2 \boldsymbol{\mathcal{M}}_{\ell j}$, $\ell, j = \{b, i\}$, and i denotes the internal nodal dofs. The vectors $\boldsymbol{\phi}_i$ and $\boldsymbol{\phi}_b$ are internal and boundary nodal displacements, respectively. By eliminating the homogeneous system of equations, Eq. (4) can be reduced to

$$\boldsymbol{\mathcal{D}}(\omega)\boldsymbol{\phi}_b = \boldsymbol{f}_b, \quad \text{with} \quad \boldsymbol{\mathcal{D}}(\omega) = \boldsymbol{\mathcal{D}}_{bb}(\omega) - \boldsymbol{\mathcal{D}}_{bi}(\omega)\boldsymbol{\mathcal{D}}_{ii}^{-1}(\omega)\boldsymbol{\mathcal{D}}_{ib}(\omega), \tag{5}$$

a transformation referred to as dynamic condensation. Due to the periodicity, the boundary nodes can be separated in a set of master (m) and slave (s) nodal dofs, referred to as master and slave Bloch-Floquet nodal dofs. The full set of master nodal dofs is represented in Fig. 1 for the unit cell considered here. Master and slave nodal dofs are related through Bloch-Floquet boundary conditions

$$\boldsymbol{\phi}_s = \Lambda(\boldsymbol{k})\boldsymbol{\phi}_m, \tag{6}$$

where $\Lambda(\boldsymbol{k})$ is a matrix containing the Bloch-Floquet vector $\boldsymbol{k}$, and the nodal coordinates $\boldsymbol{\phi}_m$ and $\boldsymbol{\phi}_s$ are the Bloch-Floquet master and slave nodal dofs, respectively, such that

$$\boldsymbol{\phi}_b = \begin{pmatrix} \boldsymbol{\phi}_m \\ \boldsymbol{\phi}_s \end{pmatrix} = \begin{pmatrix} \mathbb{1} \\ \Lambda(\boldsymbol{k}) \end{pmatrix} \boldsymbol{\phi}_m. \tag{7}$$

The Bloch-Floquet transformation matrix $\Lambda(\boldsymbol{k})$ depends on the periodicity and symmetry, and is explicitly specified in the following sections.

Similarly, we introduce master and slave boundary tractions as

$$\boldsymbol{f}_b = \begin{pmatrix} \boldsymbol{f}_m \\ \boldsymbol{f}_s \end{pmatrix}, \tag{8}$$

and we observe that, by equilibrium along the master nodes, the following equation holds

$$\boldsymbol{f}_m + \Lambda^{\mathrm{T}}(-\boldsymbol{k})\boldsymbol{f}_s = \boldsymbol{0}, \tag{9}$$

or, more compactly

$$\left(\mathbb{1}, \Lambda^{\mathrm{T}}(-\boldsymbol{k})\right)\boldsymbol{f}_b = \boldsymbol{0}. \tag{10}$$

By substitution of (7) into (5), and by left-multiplying Eq. (5) by the matrix introduced in Eq. (10), we obtain

$$(\boldsymbol{\mathcal{D}}_{mm}(\omega) + \Lambda^{\mathrm{T}}(-\boldsymbol{k})\boldsymbol{\mathcal{D}}_{sm}(\omega) + \boldsymbol{\mathcal{D}}_{ms}(\omega)\Lambda(\boldsymbol{k}) + \Lambda^{\mathrm{T}}(-\boldsymbol{k})\boldsymbol{\mathcal{D}}_{ss}(\omega)\Lambda(\boldsymbol{k}))\boldsymbol{\phi}_m = \boldsymbol{0}. \tag{11}$$

where we have segmented the matrix $\boldsymbol{\mathcal{D}}(\omega)$ in Eq. (5) according to the Bloch-Floquet master and slave nodes. We observe that finding k for any given ω and propagation angle in Eq. (11) is a non-linear eigenvalue problem defined over the Bloch-Floquet master nodes. Additionally, the matrix $\boldsymbol{\mathcal{D}}$ in Eq. (5) has been obtained via dynamic condensation, which involves a large matrix inversion for each frequency ω.

2.2. One-dimensional periodicity

For 1D periodic structures, as the one represented in Fig. 1(a), the Bloch-Floquet matrix in Eq. (6) is

$$\Lambda_{1\mathrm{D}}(k) = \exp(ik\ell)\ \mathbb{1}, \tag{12}$$

where k is the 1D Bloch wave number and ℓ is the lattice spacing. For a periodic structure with 1D translational symmetry, the direct substitution of Eq. (12) into Eq. (11) leads to the second degree polynomial eigenvalue problem

$$\left[\boldsymbol{\mathcal{D}}_{ms}(\omega)\xi^2 + (\boldsymbol{\mathcal{D}}_{mm}(\omega) + \boldsymbol{\mathcal{D}}_{ss}(\omega))\xi + \boldsymbol{\mathcal{D}}_{sm}(\omega)\right]\boldsymbol{\phi}_m = \boldsymbol{0}, \tag{13}$$

where we have introduced $\xi = \exp(ik\ell)$.

2.3. Two-dimensional periodicity

In this section, we use a similar formulation as in Mace and Manconi [23]. For unit-cell representing a lattice with 2D translation symmetry with primitive vectors $\boldsymbol{t}_1$ and $\boldsymbol{t}_2$, the Bloch-Floquet matrix in Eq. (6) has the form

$$\Lambda_{2D}(\boldsymbol{k}) = \begin{pmatrix} \xi_1 \mathbb{1}_l & \mathbb{0}_b & \mathbb{0}_{lb} \\ \mathbb{0}_l & \xi_2 \mathbb{1}_b & \mathbb{0}_{lb} \\ \mathbb{0}_l & \mathbb{0}_b & \xi_1 \mathbb{1}_{lb} \\ \mathbb{0}_l & \mathbb{0}_b & \xi_2 \mathbb{1}_{lb} \\ \mathbb{0}_l & \mathbb{0}_b & \xi_1 \xi_2 \mathbb{1}_{lb} \end{pmatrix}$$

$$= \xi_1 \mathbb{M}_1 + \xi_2 \mathbb{M}_2 + \xi_1 \xi_2 \mathbb{M}_{12}, \tag{14}$$

Table 1
Physical parameters (first ten rows) and numerical FE and reduction parameters (last four rows) for the unit cells in Fig. 1(a) and (b). The nine elastic constants (three Young's moduli, three shear moduli and three Poisson's ratios) are the redundant elastic constants which define the Voigt representation of orthotropic stiffness tensors for Duraform (first column) and Aluminum (second column).

	Unit cells	
	Fig. 1(a)	Fig. 1(b)
ρ [kg/m^3]	1100	2700
E_x [10^9 Pa]	3.03	70
E_y [10^9 Pa]	3.03	70
E_z [10^9 Pa]	1.6	70
G_{xy} [10^9 Pa]	1.14	26.3
G_{yz} [10^9 Pa]	0.87	26.3
G_{xz} [10^9 Pa]	0.87	26.3
ν_{xy}	0.33	0.33
ν_{yz}	0.33	0.33
ν_{xz}	0.33	0.33
$\omega_c/(2\pi)$ [Hz]	3128.7	122,410
N	20,484	5169
m	194	250
N_e	40% N	40% N

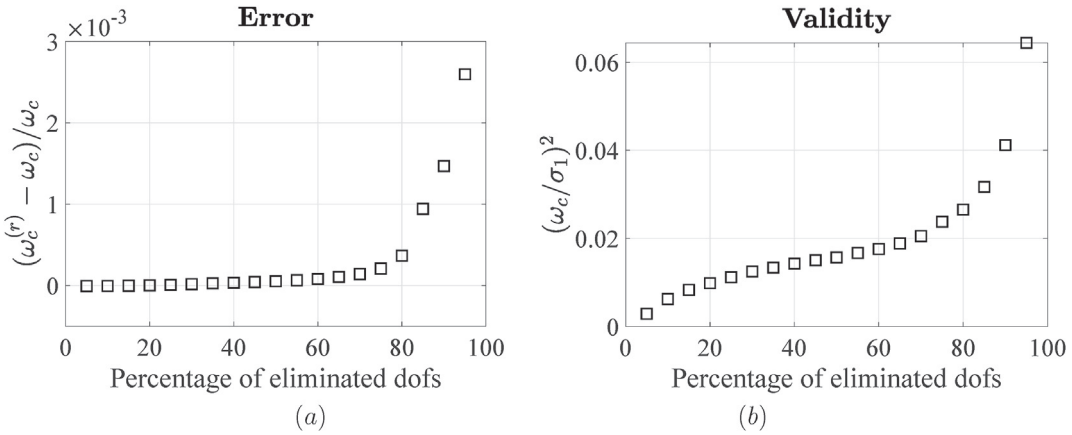

Fig. 2. Assessment of Guyan condensation for the structure represented in Fig. 1(a). In panel (a) we represent the error committed by the cut-off Guyan eigenfrequency $\omega_c^{(r)}$ with respect to the cut-off frequency for the full model (see ω_c in Table 1) as a function of the eliminated number of dofs. In panel (b) we assess the asymptotic expansion controlled by $(\omega_c/\sigma_1)^2$ as a function of the percentage of eliminated nodes.

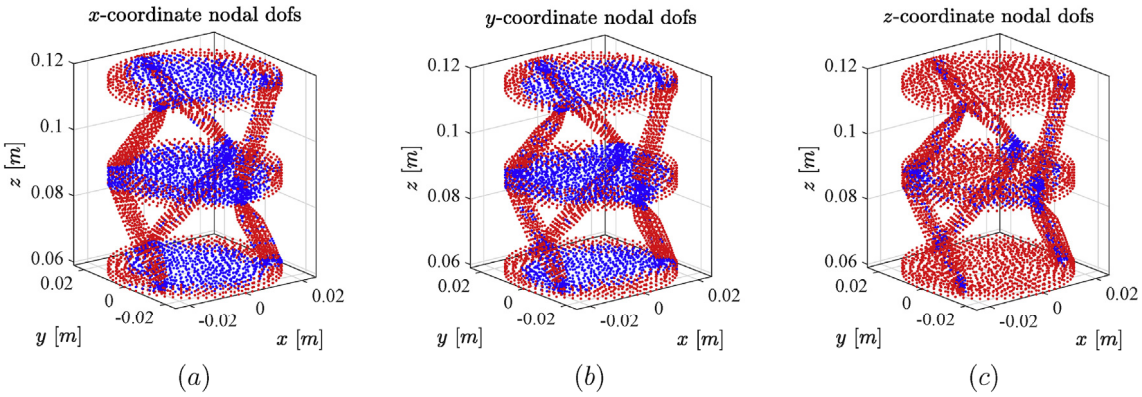

Fig. 3. Eliminated nodal dofs (blue dots) and retained nodal dofs (red dots). Panels (a), (b) and (c) refer to the $x-$, $y-$ and $z-$coordinate of the nodal dofs, respectively. The percentage of total eliminated dofs is 40% (*cf.* Fig. 2). (For interpretation of the references to color in this figure legend, the reader is referred to the Web version of this article.)

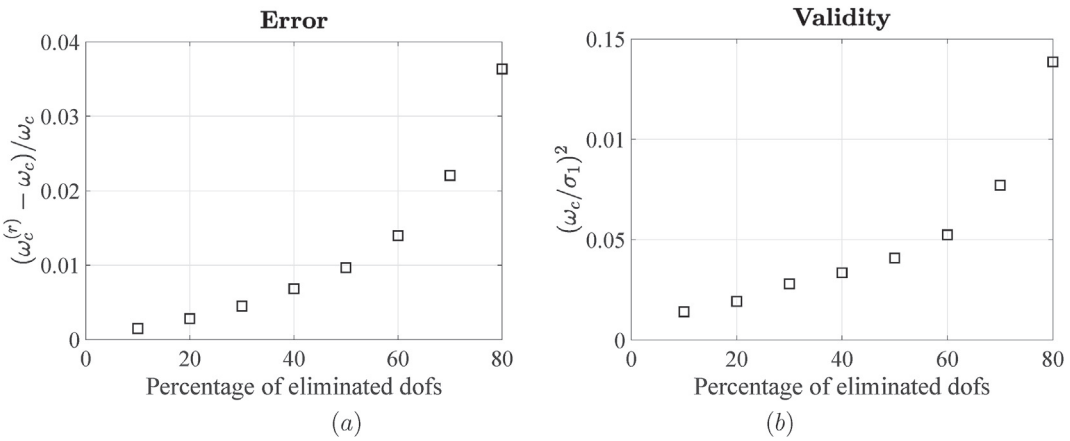

Fig. 4. Assessment of Guyan condensation for the structure represented in Fig. 1(b). In panel (a) we represent the error of the cut-off Guyan eigenfrequency $\omega_c^{(r)}$ with respect to the exact cut-off frequency $\omega_c/(2\pi) = 122,410$ Hz as a function of the eliminated number of dofs. In panel (b) we assess the asymptotic expansion via the ratio $(\omega_c/\sigma_1)^2$ as a function of the percentage of eliminated nodes.

where $\xi_1 = \exp(i\boldsymbol{k}\cdot\boldsymbol{t}_1)$ and $\xi_2 = \exp(i\boldsymbol{k}\cdot\boldsymbol{t}_2)$.

Substitution of Eq. (14) into (11) leads to the non-linear eigenvalue problem

$$\left[\mathbb{A}_0 + \xi_1\mathbb{A}_1 + \xi_2\mathbb{A}_2 + \xi_1^2\mathbb{A}_3 + \xi_2^2\mathbb{A}_4 + \xi_1\xi_2\mathbb{A}_5 + \xi_1^2\xi_2\mathbb{A}_6 + \xi_1\xi_2^2\mathbb{A}_7 + \xi_1^2\xi_2^2\mathbb{A}_8\right]\boldsymbol{\phi}_m = \mathbf{0}. \tag{15}$$

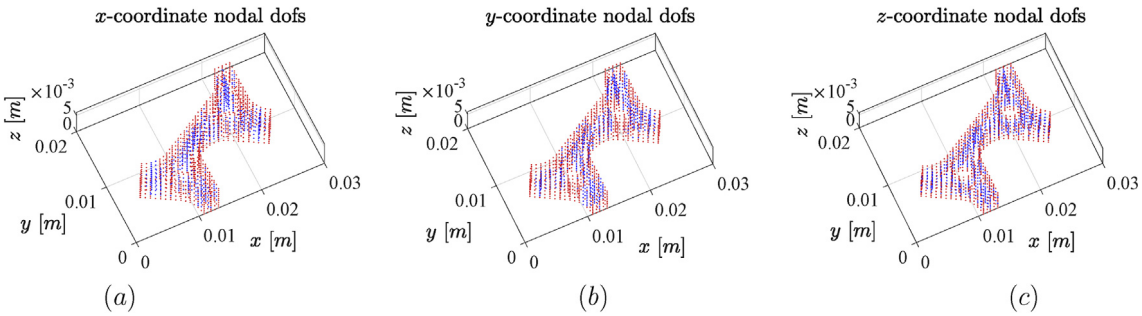

Fig. 5. Eliminated nodal dofs (blue dots) and retained nodal dofs (red dots). Panels (a), (b) and (c) refer to the $x-$, $y-$ and $z-$coordinate of the nodal dofs, respectively. The percentage of total eliminated dofs is 40% (*cf.* Fig. 4). (For interpretation of the references to color in this figure legend, the reader is referred to the Web version of this article.)

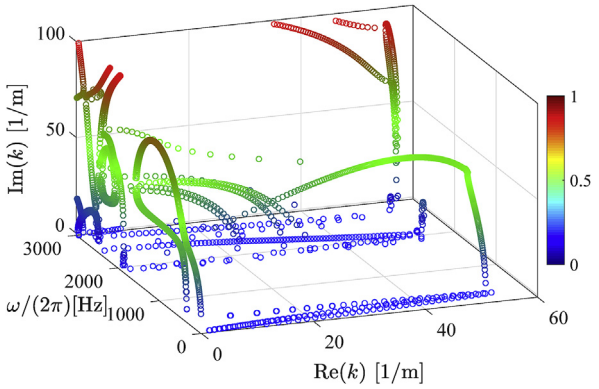

Fig. 6. Dispersion diagram for the 1D periodic structure whose unit-cell is represented in Fig. 1(a) calculated using the Guyan superelement for the DSM, with parameters listed in Table 1. Calculated real and imaginary parts of k are represented as a function of frequency. The color map $\xi \in [0,1]$ is such that $\mathrm{Im}(k) = \xi\, k_{\max}$, with $k_{\max} = 1001/\mathrm{m}$. (For interpretation of the references to color in this figure legend, the reader is referred to the Web version of this article.)

The definition of the matrices $\mathbb{A}_i, i = \{0,\dots,8\}$ can be readily obtained from (15). In the special case when voids are present in the geometry, it is convenient to choose the unit cell edges such that the voids are located at the corner points. This reduces the degree of the polynomial in ξ_1 and ξ_2 in Eq. (15) to

$$\left[\xi_1\overline{\mathbb{A}}_1 + \xi_2\overline{\mathbb{A}}_2 + \xi_1^2\overline{\mathbb{A}}_3 + \xi_2^2\overline{\mathbb{A}}_4 + \xi_1\xi_2\overline{\mathbb{A}}_5 + \xi_1^2\xi_2\overline{\mathbb{A}}_6 + \xi_1\xi_2^2\overline{\mathbb{A}}_7\right]\boldsymbol{\phi}_m = \mathbf{0}. \tag{16}$$

The definitions of the matrices $\overline{\mathbb{A}}_i, i = \{1,\dots,7\}$ can be obtained suppressing the corner nodal coordinates in the Bloch matrix in Eq. (14).

Triangular lattice. The primitive vectors of a triangular lattice are

$$\boldsymbol{t}_1 = \ell\begin{pmatrix}1\\0\end{pmatrix}, \quad \boldsymbol{t}_2 = \frac{\ell}{2}\begin{pmatrix}1\\\sqrt{3}\end{pmatrix}, \tag{17}$$

which leads to

$$\begin{aligned}\xi_1 &= \exp(i\boldsymbol{t}_1\cdot\boldsymbol{k}) = \exp(ik\ell\cos\vartheta),\\ \xi_2 &= \exp(i\boldsymbol{t}_2\cdot\boldsymbol{k}) = \exp\left[ik\ell(\cos\vartheta+\sqrt{3}\sin\vartheta)/2\right].\end{aligned} \tag{18}$$

For special values of the propagation angle ϑ such that

$$\frac{1}{2}\left(1+\sqrt{3}\tan\vartheta\right) = m_2/m_1, \quad \text{with } m_1, m_2 \in \mathbb{Z}, \tag{19}$$

Eq. (18) can be rewritten as

$$\xi_1 = \gamma^{m_1} \quad \text{and} \quad \xi_2 = \gamma^{m_2}, \tag{20}$$

with $\gamma = \exp(ik\ell)$. The high-symmetry points in the first Brillouin zone of a triangular lattice are

$$\boldsymbol{\Gamma} = \begin{pmatrix}0\\0\end{pmatrix}, \quad \mathbf{M} = \frac{2\pi}{\sqrt{3}\ell}\begin{pmatrix}0\\1\end{pmatrix}, \quad \mathbf{K} = \frac{2\pi}{3\ell}\begin{pmatrix}1\\\sqrt{3}\end{pmatrix}.$$

For $\mathrm{Re}(\boldsymbol{k}) \in \mathbf{MK}$, a segment of the irreducible Brillouin zone for the triangular lattice, we assume that $\boldsymbol{k} = \mathbf{M} + \boldsymbol{\kappa}$, with $\boldsymbol{\kappa} = (\kappa, 0)^{\mathrm{T}}$. Therefore, we obtain

$$\xi_1 = \gamma, \quad \text{and} \quad \xi_2 = -\gamma^{1/2}, \quad \text{for} \quad \mathrm{Re}(\boldsymbol{k}) \in \mathbf{MK}. \tag{21}$$

3. Numerical reduction of the unit cell

3.1. Guyan condensation

The full dynamic stiffness matrix for the boundary nodes is given in Eq. (5). As mentioned earlier, it involves the inversion of a (large) matrix. Such inversion needs to be performed at every frequency step considered in Eq. (11). It would be desirable to reduce the size of the matrix to be inverted, with minimal loss of accuracy. To do so let us consider two sets of nodal dofs for

which $\boldsymbol{U} = (\boldsymbol{U}_r, \boldsymbol{U}_e)^{\mathrm{T}}$ and the corresponding block partitions of the mass and stiffness matrices, $\boldsymbol{\mathcal{M}}_{ij}$ and $\boldsymbol{\mathcal{K}}_{ij}$, with $i,j = \{r,e\}$. The subscript "r" and "e" denote retained and eliminated, respectively. The displacement vectors are such that $\boldsymbol{U}_r \in \mathbb{C}^{N_r}$ and $\boldsymbol{U}_e \in \mathbb{C}^{N_e}$, with $N_e + N_r = N$. The dynamic stiffness matrix for the retained nodes $\boldsymbol{U}_r$ is

$$\overline{\boldsymbol{\mathcal{D}}}(\omega) = \boldsymbol{\mathcal{D}}_{rr}(\omega) - \boldsymbol{\mathcal{D}}_{re}(\omega)\boldsymbol{\mathcal{D}}_{ee}^{-1}(\omega)\boldsymbol{\mathcal{D}}_{er}(\omega). \tag{22}$$

Guyan condensation [37] relies on the expansion of $\boldsymbol{\mathcal{D}}_{ee}^{-1}(\omega)$ in Eq. (22) up to $O(\omega^2)$. It results in

$$\overline{\boldsymbol{\mathcal{D}}}(\omega) = \boldsymbol{\mathcal{D}}_{\mathrm{G}}(\omega) + O(\omega^4), \tag{23}$$

with

$$\begin{aligned} &\boldsymbol{\mathcal{D}}_{\mathrm{G}} = \boldsymbol{\mathcal{K}}_{\mathrm{G}} - \omega^2 \boldsymbol{\mathcal{M}}_{\mathrm{G}}, \quad \boldsymbol{\mathcal{K}}_{\mathrm{G}} = \boldsymbol{\mathcal{K}}_{rr} - \boldsymbol{\mathcal{K}}_{re}\boldsymbol{\mathcal{K}}_{ee}^{-1}\boldsymbol{\mathcal{K}}_{er}, \\ &\boldsymbol{\mathcal{M}}_{\mathrm{G}} = \boldsymbol{\mathcal{M}}_{rr} - \boldsymbol{\mathcal{K}}_{re}\boldsymbol{\mathcal{K}}_{ee}^{-1}\boldsymbol{\mathcal{M}}_{er} - \boldsymbol{\mathcal{M}}_{re}\boldsymbol{\mathcal{K}}_{ee}^{-1}\boldsymbol{\mathcal{K}}_{er}, \end{aligned} \tag{24}$$

where the last two equations are Guyan stiffness and mass matrices. Inspired by Ref. [44], the following identity holds

$$\begin{aligned} \boldsymbol{\mathcal{D}}_{ee}^{-1}(\omega) &= \left(\boldsymbol{\mathcal{K}}_{ee} - \omega^2 \boldsymbol{\mathcal{M}}_{ee}\right)^{-1} \\ &= \left[\mathbb{1} + \omega^2 \overline{\boldsymbol{\mathcal{V}}}\left(\Sigma - \omega^2 \mathbb{1}\right)^{-1} \overline{\boldsymbol{\mathcal{V}}}^{\mathrm{T}}\right] \boldsymbol{\mathcal{K}}_{ee}^{-1}, \end{aligned} \tag{25}$$

where

$$\left(\boldsymbol{\mathcal{K}}_{ee} - \sigma_\nu^2 \boldsymbol{\mathcal{M}}_{ee}\right) \overline{\boldsymbol{U}}_\nu = \boldsymbol{0}, \quad \nu = 1, \ldots, N_e,$$

$$\text{with} \quad \overline{\boldsymbol{\mathcal{V}}}^{\mathrm{T}} \boldsymbol{\mathcal{M}}_{ee}^{-1} \boldsymbol{\mathcal{K}}_{ee} \overline{\boldsymbol{\mathcal{V}}} = \mathrm{diag}(\sigma_\nu) \equiv \Sigma, \quad \text{and} \quad \overline{\boldsymbol{\mathcal{V}}} = \left[\overline{\boldsymbol{U}}_1 \cdots \overline{\boldsymbol{U}}_{N_e}\right]. \tag{26}$$

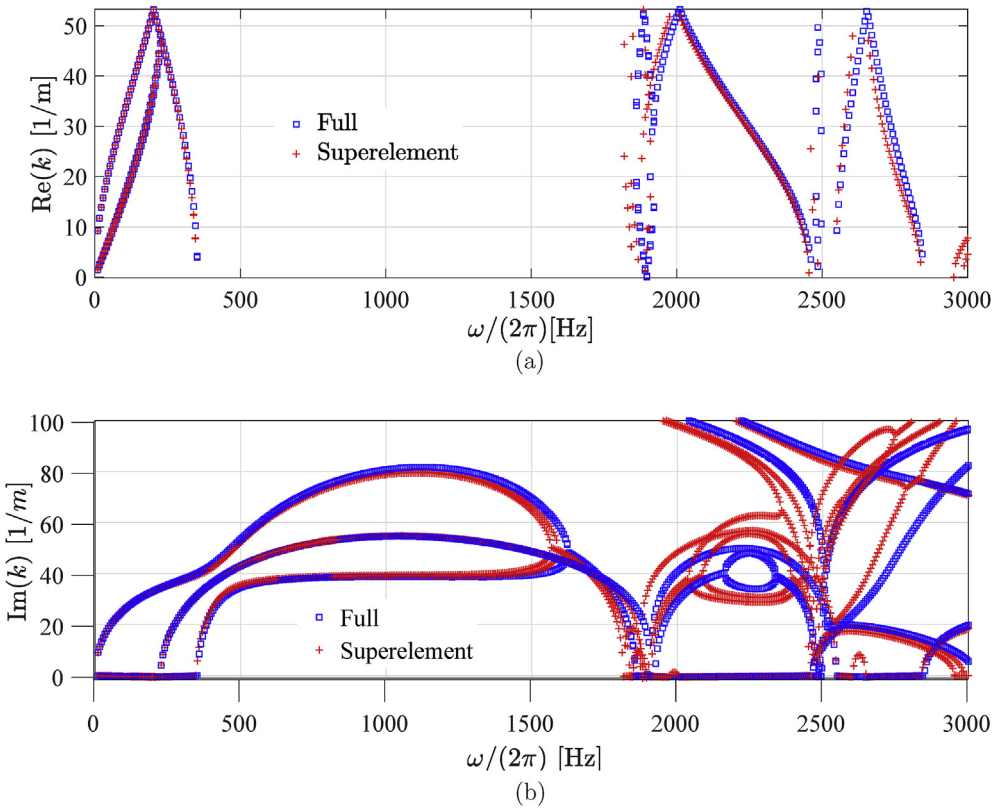

Fig. 7. Comparison of full dispersion (blue squares) and dispersion obtained via Guyan superelement of the unit cell in Fig. 1(a). Panel (a) and (b) refer to the real and imaginary part of k, respectively, as a function of frequency. The superelement has been obtained by eliminating the 40% of the total dofs. (For interpretation of the references to color in this figure legend, the reader is referred to the Web version of this article.)

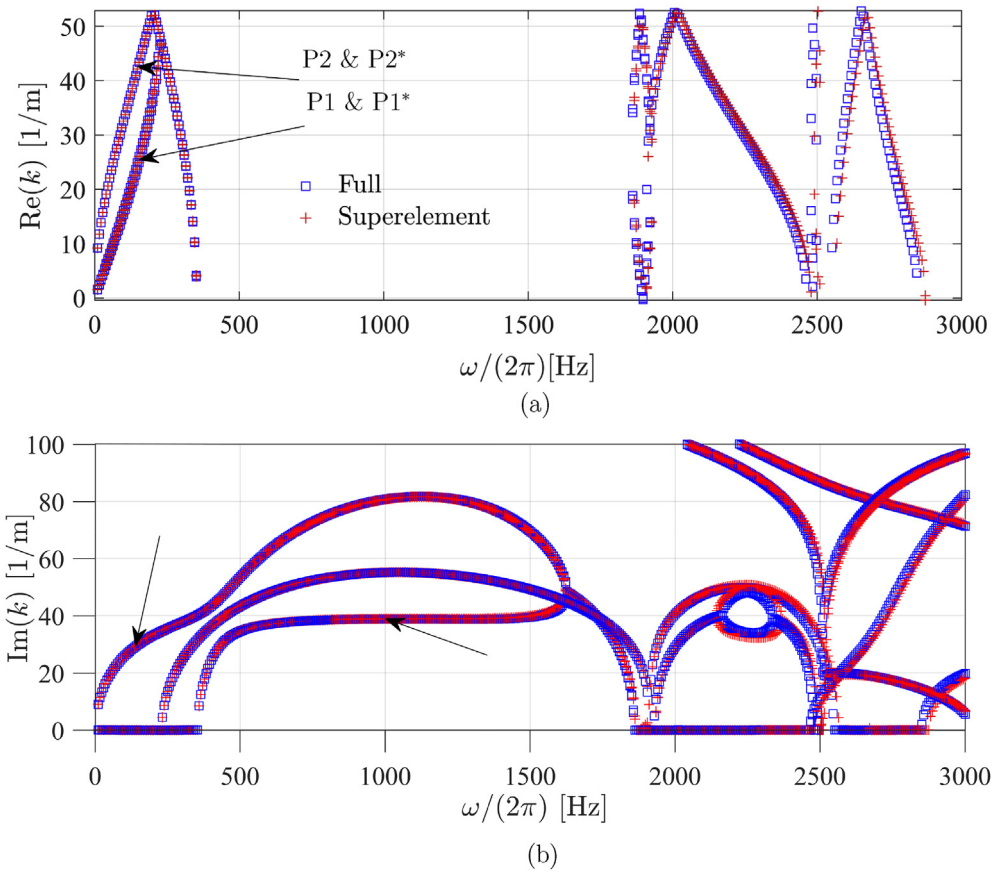

Fig. 8. Comparison of full dispersion (blue squares) and dispersion obtained via Guyan superelement of the unit cell in Fig. 1(a). Panel (a) and (b) refer to the real and imaginary part of k, respectively, as a function of frequency. The superelement has been obtained by eliminating the 95% of the internal nodal dofs and including the full set of Bloch-Floquet master dofs. (For interpretation of the references to color in this figure legend, the reader is referred to the Web version of this article.)

Exploiting the fact that Σ in Eq. (26) is a diagonal matrix, the identity in Eq. (25) becomes

$$\left(\boldsymbol{D}_{ee}^{-1}\right)_{ij} = \left(\boldsymbol{K}_{ee}^{-1}\right)_{ij} + \sum_{\ell m} \overline{\boldsymbol{U}}_{im}\overline{\boldsymbol{U}}_{\ell m}\frac{\omega^2}{\sigma_m^2}\frac{\left(\boldsymbol{K}_{ee}^{-1}\right)_{\ell j}}{1-\omega^2/\sigma_m^2}. \tag{27}$$

Eq. (27) clearly shows that Guyan condensation (23) is accurate if

$$\omega^2/\sigma_1^2 \ll 1, \tag{28}$$

where σ_1 is the smallest eigenvalue of the eigenvalue problem in Eq. (26). In addition Eq. (27) provides the connection between modal based reduction methods [35,36] with expansion based techniques [37]. In the present paper we will focus on the latter one. We still did not specify an algorithm for the elimination of nodal dofs in such a way that Eq. (28) is satisfied. In the next section, we provide an algorithmic partition of the unit cell nodal dofs which satisfies the condition (28).

3.2. Selection of retained nodal dofs

The selection of eliminated nodal dofs such that (28) is satisfied follows a statistical approach referred to as *effective independent distribution vector* procedure [45,46]. It relies on the construction of the Fisher information matrix

$$\boldsymbol{\mathcal{F}} = [\boldsymbol{\mathcal{U}}]_{ap}^{\mathrm{T}}[\boldsymbol{\mathcal{U}}]_{ap}, \tag{29}$$

where $[\cdot]_{ap}$ denotes selection of a set of rows with indices $a \in \mathbb{N}^n/0$, where $n \leq N$ is a nonzero natural number, and a set of columns with indices $p = \{1, 2.., m\}$, $m < N$ being a non-zero natural number. It is important to observe that a corresponds to a selection of nodal dofs and p are the indices of the eigenmodes associated with the first m eigenvalues. At the beginning $a = \{1, 2, \dots, N\}$, *i.e.* all nodal dofs are included. The procedure continues with the construction of the idempotent matrix

$$\boldsymbol{\mathcal{E}} = [\boldsymbol{\mathcal{U}}]_{ap}\boldsymbol{\mathcal{F}}^{-1}[\boldsymbol{\mathcal{U}}]_{ap}^{\mathrm{T}}, \tag{30}$$

whose trace equals its rank. Hence, terms on the diagonal of the matrix $\boldsymbol{\mathcal{E}}$ represent the fractional contribution of the nodal dofs to the rank of $\boldsymbol{\mathcal{E}}$, i.e. to the linear independence of the first m eigenvectors. The procedure continues by analyzing the diagonal of the matrix (30) and finding the indices of the entries that contribute the least to rk($\boldsymbol{\mathcal{E}}$). After the elimination of the nodal dof (i.e. the elimination of the corresponding element in the set a in Eq. (29)) the procedure continues until a desired amount of nodal dofs N_e has been eliminated ($N_r = N - N_e$).

3.3. Accuracy of Guyan condensation for the free eigenvalue problem

After we have established a selection procedure for the slave nodes in section 3.2, we can assess the quality of Guyan approximation. We start by choosing a cut-off frequency ω_c, for example belonging to the spectrum of the free eigenvalue problem for the considered unit cell. Two unit cells are analysed, whose geometry is represented in Fig. 1 and whose material and discretisation parameters are summarised in Table 1. It is useful to introduce the free eigenvalue problem defined over the reduced Guyan mass and stiffness matrices

$$\left[\boldsymbol{\mathcal{K}}_{\mathrm{G}} - \left(\omega_i^{(r)}\right)^2 \boldsymbol{\mathcal{M}}_{\mathrm{G}}\right] \mathbf{r}_i = \mathbf{0}, \quad i = \{1, \ldots, N_r\}. \tag{31}$$

The structures in Fig. 1 have been meshed using ANSYS Workbench 18.2. The physical parameters associated with the structures in Fig. 1(a) and (b) are reported in Table 1 and correspond to duraform and aluminum, respectively. In Fig. 2(a) we compare the cut-off frequency ω_c of the full model (see Table 1) to the corresponding eigenfrequency $\omega_c^{(r)}$, obtained solving the Guyan eigenvalue problem in Eq. (31) as a function of the percentage of eliminated dofs N_e via the procedure described in section 3.2. The elimination procedure seeks for the linear independence of the set of the lowest m eigenmodes for the structure (see Table 1). Fig. 2(a) demonstrates that the eigenfrequencies with free boundary conditions for the structure in Fig. 1(a) can be obtained by the Guyan eigenvalue problem (31). In Fig. 2(b) we assess the condition in Eq. (28) for several percentages of eliminated dofs and show that such condition is satisfied up to 95% of eliminated nodes. Eliminated (blue dots) and retained (red dots) nodal dofs for the structure in Fig. 1(a) are represented in Fig. 3, where in panels (a), (b) and (c) are the three Cartesian component of the nodal displacement. The amount of eliminated nodal dofs N_e is given in Table 1. We observe that the retained nodes (red dots) as predicted by the procedure in section 3.2, accumulate in proximity of the circumference of the disks and along the beams. Similar conclusions apply for Fig. 4 where we estimate the Guyan eigenfrequency error and the validity of Eq. (28) for the structure in Fig. 1(b). In Fig. 4, the elimination procedure spans from 10% to 80% of the total dofs and uses the first

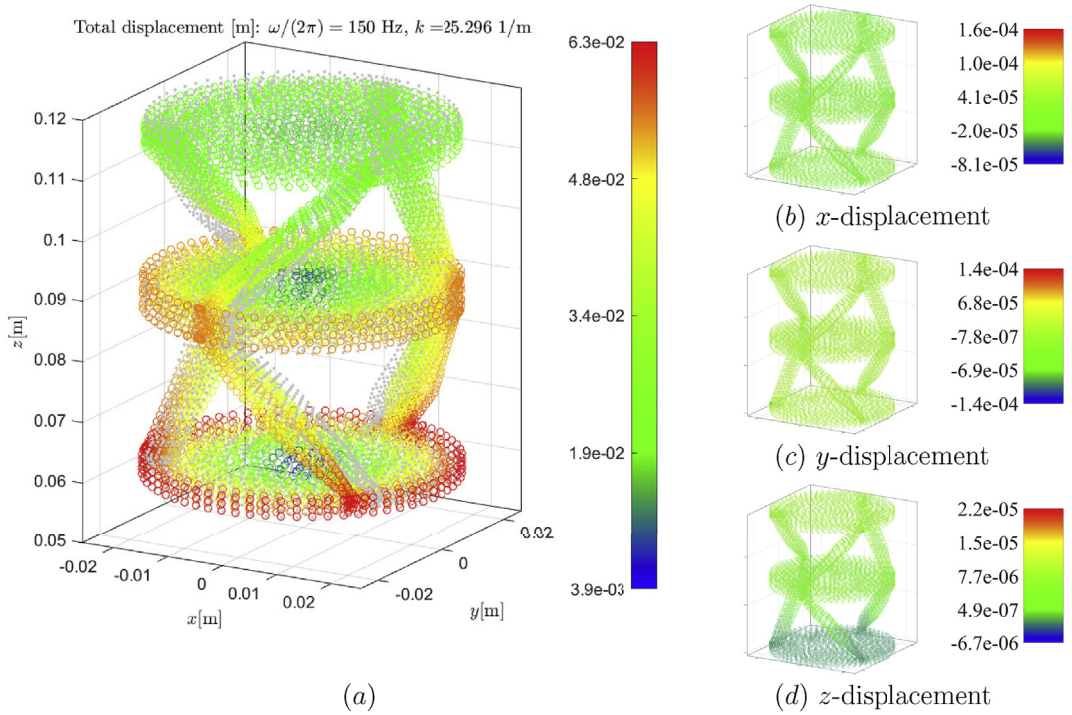

Fig. 9. Propagating eigenmodes corresponding to the P1 point in Fig. 8(a). The color map in panel (a) represents the norm of the eigenmode (colored hollow circles) nodal displacement with overlaid total nodal displacement (scale 0.08) with respect to the undeformed nodes (grey dots). Panels (b)–(d) represent the difference between the full and reduced eigenmode (x-, y- and z-component of the displacement, respectively). The wave number corresponding to the reduced model is $k = 25.295$ [1/m]. (For interpretation of the references to color in this figure legend, the reader is referred to the Web version of this article.)

m free eigenmodes (see Table 1) for the free structure - up to 800 kHz. With reference to Fig. 5, we observe that, for a 40% level of elimination, retained nodal dofs (red dots) accumulate mainly at the boundaries of the unit cell and along the holes. Those nodal dofs are the ones that contribute the most to the linear independence of the eigenmodes.

4. Results and discussion

In this section we use Guyan condensation calculated over the retained nodal dofs obtained according to the procedure described in section 3.2, for the computation of the direct Bloch-Floquet dispersion diagram of the unit cells in Fig. 1. The reduced mass and stiffness matrices defined in Eq. (24) define a Guyan superelement.

The use of Guyan superelement allows reducing the computational demand of both the dynamic condensation in Eq. (5) and the quadratic eigenvalue problem in Eq. (13). Such reduction can be traced back to the reduced amount of both internal and Bloch-Floquet master nodes retained after the elimination procedure (see Figs. 3 and 5). An important part of the problem is the

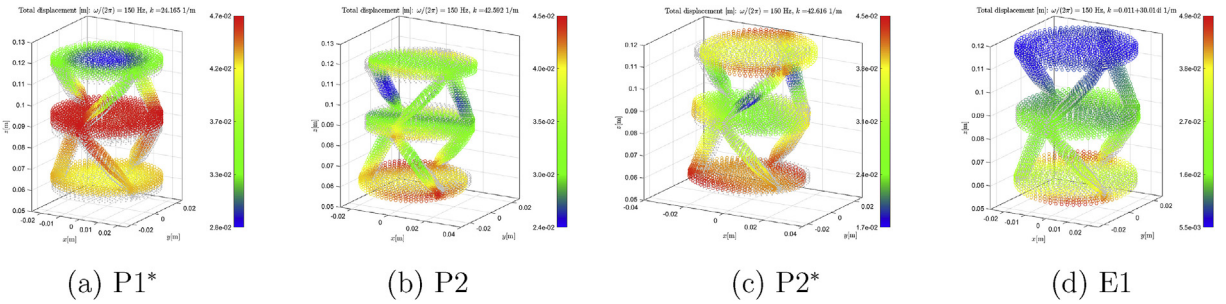

Fig. 10. Eigenmodes corresponding to 150 Hz. Panels (a)–(c) are full propagating eigenmodes corresponding to the wave vectors P1*, P2 and P2* of Fig. 8(a), respectively. Panel (d) represents the complex eigenmode E1 (see Fig. 8(b)) in the pass-band. Color maps and markers have the same meaning as in Fig. 9(a). (For interpretation of the references to color in this figure legend, the reader is referred to the Web version of this article.)

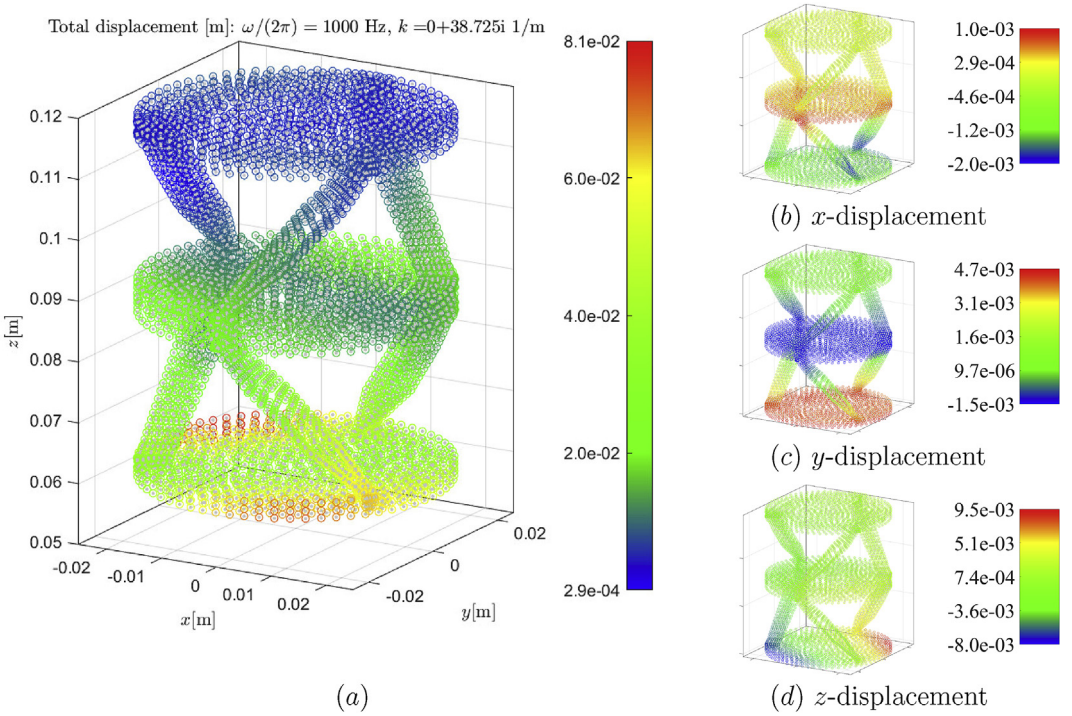

Fig. 11. Evanescent eigenmodes corresponding to the E2 point in Fig. 8(b). The color map in panel (a) represents the norm of the eigenmode with overlaid total nodal displacement (scale 10^{-3}) with respect to the non-deformed FE nodes (grey dots). Panels (b)–(d) represent the difference between the full and reduced eigenmode (x-, y- and z-component of the displacement, respectively). The wave number corresponding to the reduced model is $k = 38.817i$ [1/m]. (For interpretation of the references to color in this figure legend, the reader is referred to the Web version of this article.)

retrieval of the Bloch-Floquet eigenmodes over the eliminated nodal coordinates $\boldsymbol{U}_e$. Following section 3.1, we can write

$$\begin{aligned}\boldsymbol{U}_e &= -D_{ee}^{-1}(\omega)D_{er}(\omega)\boldsymbol{U}_r \\ &= -\left[K_{ee}^{-1}K_{er} + \omega^2\left(-K_{ee}^{-1}M_{er} + K_{ee}^{-1}M_{ee}K_{ee}^{-1}K_{er}\right)\right]\boldsymbol{U}_r + O(\omega^4),\end{aligned} \tag{32}$$

where, in the second row we have Taylor-expanded $D_{ee}^{-1}(\omega)$ and retained terms up to order $O(\omega^2)$. In the following we present dispersion diagrams calculated using the reduced DSM and corresponding selected eigenmodes calculated using Eq. (32), compare them to those obtained using the full DSM and give performance details in terms of computational time. We observe that identical computational resources have been used for the presented results, *i.e.* an 8-cores computer (Intel i7-7700, 3.60 GHz) with 44 GB of RAM. The codes have been implemented in Matlab without explicit parallelisation of the problem.

1D periodicity. Let us focus on the unit cell in Fig. 1(a), with material parameters listed in Table 1 and lattice spacing $\ell = 0.059$ m. In Fig. 6 we represent the complex wave number obtained using the 40% reduced Guyan superelement in Eq. (13), and solving this equation for several frequencies. The calculated wave number is decomposed into its real and imaginary parts in such a way that each point in Fig. 6 is identified by a triplet $(\omega, \mathrm{Re}(k), \mathrm{Im}(k))$. The color highlights the imaginary part of the wave number. We observe the presence of a complete band-gap, *i.e.* a frequency range where purely imaginary wave

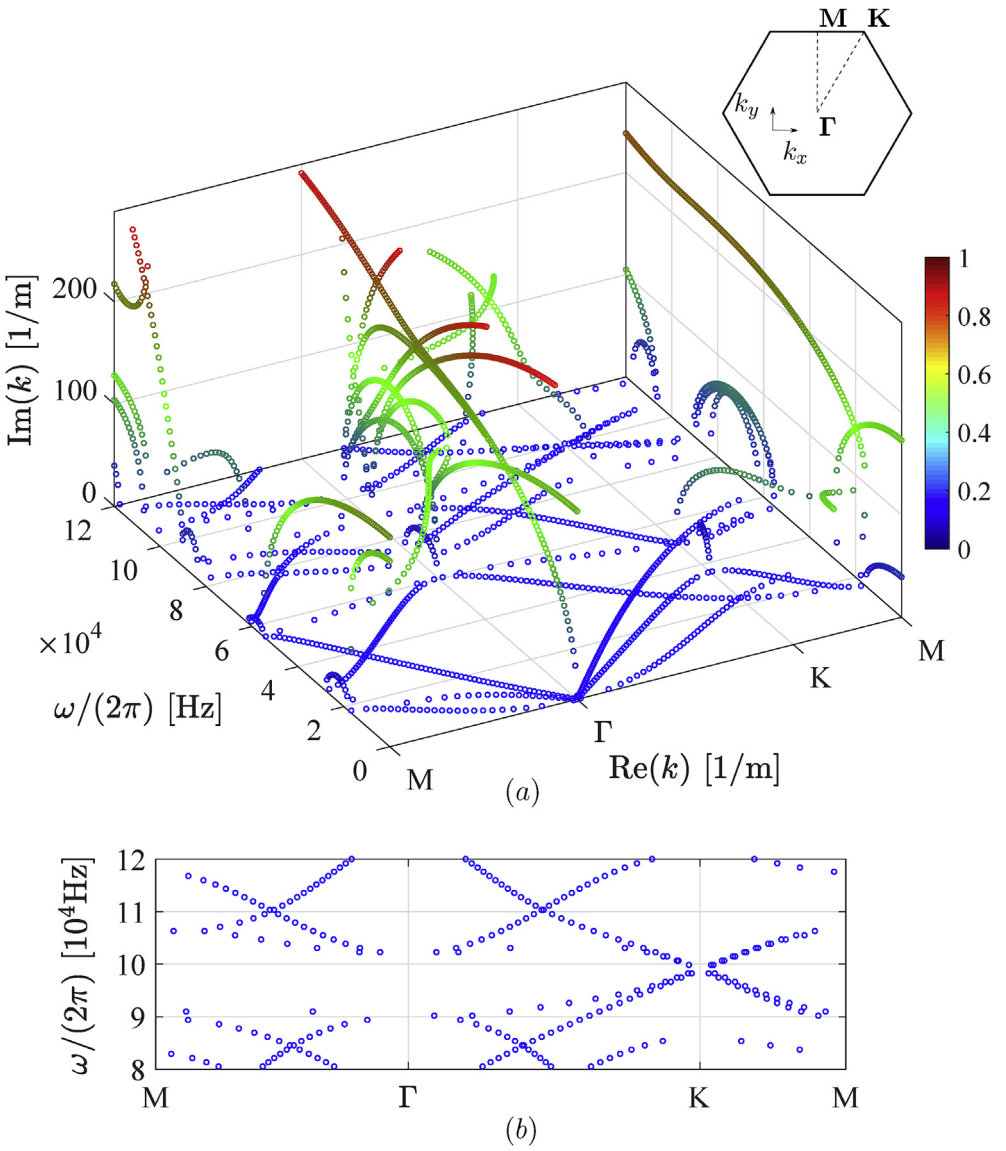

Fig. 12. Dispersion diagram associated with the unit cell in Fig. 1(b) calculated using the Guyan superelement for the DSM, with parameters listed in Table 1. Calculated real and imaginary parts of k are represented as a function of frequency. The real part of k is mapped onto the irreducible Brillouin zone path **M**Γ*KM*, represented in the top-right inset. The color map $\xi \in [0, 1]$ is such that $\mathrm{Im}(k) = \xi\, k_{\max}$, with $k_{\max} = 288.21/\mathrm{m}$. (For interpretation of the references to color in this figure legend, the reader is referred to the Web version of this article.)

numbers are obtained. As discussed in Ref. [43], the band-gap is associated with tacticity, *i.e.* the relative arrangement of geometrically chiral elements within a single unit cell.

In Fig. 7 we compare the dispersion calculation using the full DSM (blue squares) with the dispersion obtained using Guyan superelement (red crosses). The data associated with red crosses are the same as in Fig. 6. Panels (a) and (b) refer to the real and imaginary parts as a function of frequency. The figures show a good agreement with gradually decreasing accuracy as the frequency approaches the cut-off frequency for Guyan superelement construction. The frequency sampling comprises 500 frequency points. The dispersion for the full model was obtained in 16.1 h, of which 46% required by the dynamic condensation of the full DSM and 54% by the quadratic eigenvalue problem defined over the full set of master nodes. The dispersion obtained from the Guyan superelement runs in 3.6 h - a reduction of more than 75% in computational time - of which 42% required by the dynamic condensation of the Guyan DSM and 58% by the solution of the quadratic eigenvalue problem defined over the reduced set of Bloch-Floquet master nodes. In Fig. 8 we consider the eigenvalue problem in Eq. (13) defined over the full DSM (blue squares) and over a superelement obtained eliminating 95% of internal dofs and retaining the full set of Bloch-Floquet master dofs.

Fig. 9(a) shows a propagating full Bloch-Floquet eigenmode (see P1 point in Fig. 8(a)). The color map for the hollow circles refers to the norm of the nodal displacement (with scale 10^{-3}) with respect to the equilibrium FE dots (grey dots). Panels (b)-(d) represent the full-reduced difference between the *x*-,*y*- and *z*-components of the displacement, respectively, where the used color maps refer to such difference. The eigenmode components corresponding to the reduced Bloch-Floquet calculation have been obtained by evaluating Eq. (32), with $\boldsymbol{U}_r$ being that resulting from Fig. 8. The figures demonstrate that the eigenmode

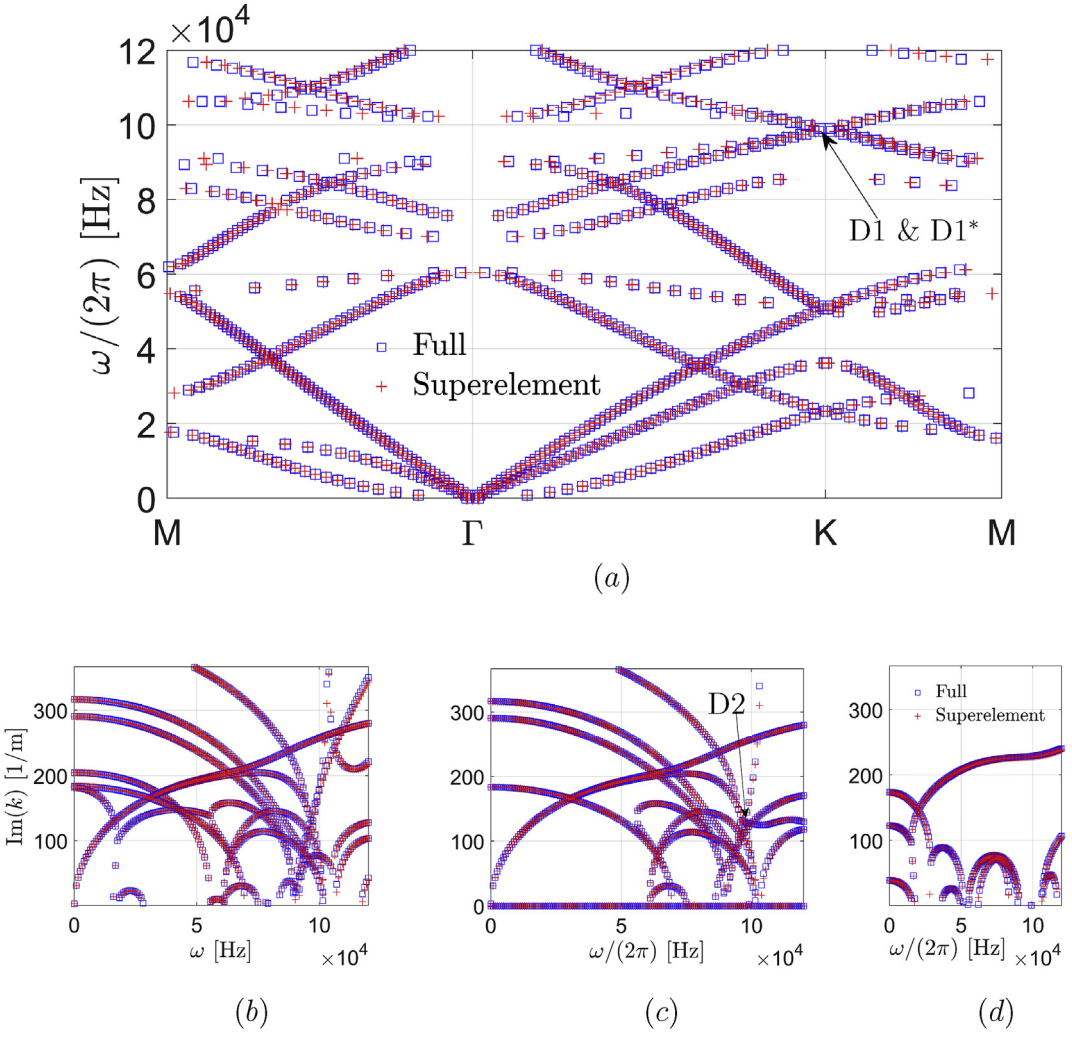

Fig. 13. Comparison of full dispersion (blue squares) and dispersion obtained via Guyan superelement of the unit cell in Fig. 1(b). Panel (a) refers to the real part of the wave vector projected over the edge of the irreducible Brillouin zone. Panels (*b*), (*c*) and (*d*) refer to the imaginary part of *k*, for real parts belonging to the **M**$\boldsymbol{\Gamma}$, $\boldsymbol{\Gamma}$*M* and **K***M* segments, respectively. The full DSM and the superelement have been obtained using the parameters in Table 1. (For interpretation of the references to color in this figure legend, the reader is referred to the Web version of this article.)

obtained with the reduced model is in agreement with the full model.

Fig. 10 shows the remaining eigenmodes (P1*, P2, P2* and E1) marked in Fig. 8. We observe that P1&P1* and P2&P2* are - within the full mesh accuracy - two couples of quasi-degenerate propagating Bloch eigenmodes, whereas E1 is an evanescent eigenmode. In Fig. 10, the comparison with the reduced eigenmodes Cartesian components has been omitted because it showed to be as accurate as those already shown in Fig. 9. Fig. 8(a)–(c) are propagating eigenmodes which show a clear coupling between longitudinal and shear deformations of the beam with the rotational degree of freedom of the disk, both around the $z-$ axis (see Figs. 9(a) and 10(a)) and around axes in the $xy-$plane (see Fig. 10(b) and (c)). In addition, Fig. 10(d) shows an eigenmode with a high imaginary part wave-number which displays a strong amplitude decay along the axis of the structure. In Fig. 11(a), we show the norm of the total nodal displacement for the evanescent band-gap eigenmode E2 in Fig. 8(b). The full-reduced difference of the nodal displacements (see the Cartesian components in Fig. 11(b)–(d)) clearly show that the superelement computation is accurate. As already mentioned, while indirect methods allow to calculate a set of Bloch eigenfrequencies and corresponding propagating eigenmodes with *real* wave vector or number in the first Brillouin zone, the direct method used here and its corresponding reduction results in *both* propagating and evanescent eigenmodes as a function of frequency (see Figs. 9 and 11).

Triangular lattice and Dirac cone. We consider here the unit cell in Fig. 1(b) and its periodic repetition according to a triangular lattice identified by the lattice vectors in Eq. (17) with lattice spacing $\ell = 0.0205$ m. We calculate the dispersion diagram for such a structure solving the eigenvalue problem in Eq. (16), where a reduced Guyan superelement (40% elimination level, see Fig. 5) is used instead of the full DSM. The results of the computations are reported in Fig. 12(a), where every point is identified by a triplet $(\omega, \mathrm{Re}(k), \mathrm{Im}(k))$. The unit cell was designed in Refs. [7] to give rise to a double Dirac cone at the high-symmetry point **K**. The double Dirac cone is highlighted Fig. 12(b) which has been obtained from the main figure by filtering the real part of the wave vector. In Fig. 13 we compare the dispersion diagram obtained using the full DSM (blue squares) to that obtained using the superelement (red crosses). Both the real part (panel (a)) and imaginary part (panels (b), (c) and (d)) of the modulus of the wave vectors agree very well in the considered frequency interval, up to the cut-off frequency for the Guyan superelement (see Table 1). We remark that the Guyan superelement is able to reproduce the double Dirac cone as predicted by the full DSM. We observe that high-frequency Dirac cones are very mesh sensitive and, to the best of our knowledge, this is the first time that a Dirac cone is retrieved using a reduced model. In addition, for 150 frequency steps, we observe time saving (reduction by a factor of 2/3) in using the Guyan superelement compared to the full DSM. In fact, the dispersion obtained from the full DSM requires 43.3 min to run, of which 66% by the dynamic condensation of the full DSM and 34% by the solution of the polynomial eigenvalue problems. The reduced model runs in 16 min, of which 12% is required by the dynamic condensation of the Guyan DSM and 88% by the solution of the non-linear eigenvalue problem defined over the corresponding reduced set of Bloch-Floquet master nodal dofs.

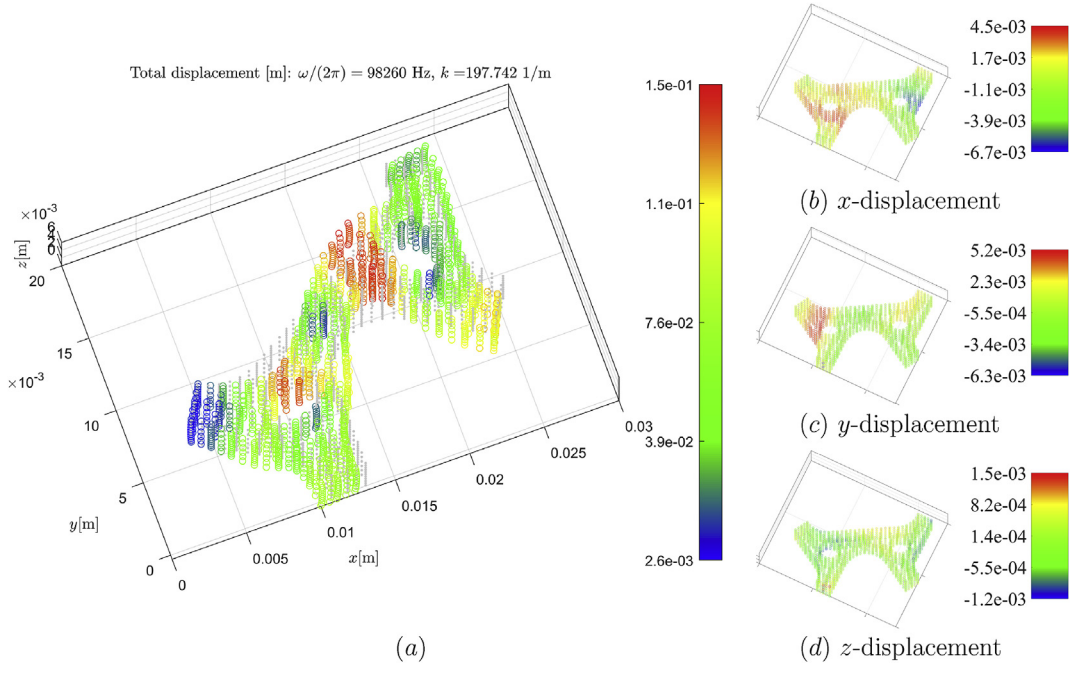

Fig. 14. Propagating eigenmodes corresponding to the D1 point in Fig. 13(a). The color map in panel (a) represents the norm of the eigenmode total nodal displacement (scale 10^{-2}) with respect to the non-deformed FE nodes (grey dots). Panels (b)–(d) are the difference between the full and reduced eigenmode (x-, y- and z-component of the displacement, respectively). The wave number corresponding to the reduced model is $k = 196.03$ [1/m]. (For interpretation of the references to color in this figure legend, the reader is referred to the Web version of this article.)

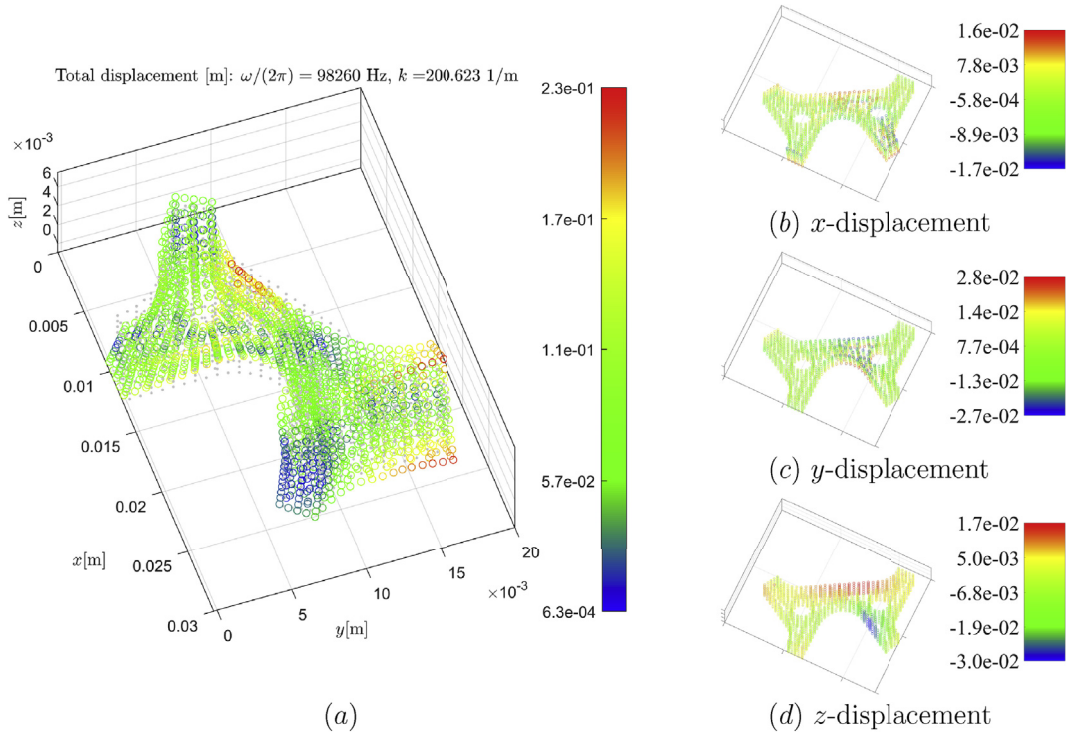

Fig. 15. Propagating eigenmode corresponding to the D1* point in Fig. 13(a). The color map in panel (a) represents the norm of the eigenmode total nodal displacement (scale 10^{-2}) with respect to the equilibrium FE nodes (grey dots). Panels (b), (c) and (d) are the difference between the full and reduced (see Eq. (32)) eigenmode x-, y- and z-component of the displacement, respectively. The wave number corresponding to the reduced model is $k = 198.54$ [1/m]. (For interpretation of the references to color in this figure legend, the reader is referred to the Web version of this article.)

In Figs. 14 and 15 we focus on the D1 and D1* propagating eigenmodes in the vicinity of the double Dirac cone in Fig. 13(a) (note that $k \approx |\mathbf{K}|$). Each eigenmode has been obtained along the direction $\mathbf{\Gamma K}$ which corresponds to Bloch waves propagating along the direction $\vartheta = \pi/3$ in the structure. As already pointed out in Refs. [7], the dynamic response around the double Dirac cone is characterised by an in-plane dominated (Fig. 14(a)) and an out-of-plane dominated eigenmode (Fig. 15(a)). As shown in Fig. 14(b)–(d) and in Fig. 15(b)–(d), the Cartesian components of the reduced eigenmode nodal displacement - obtained evaluating Eq. (32) - agree very well with the full eigenmode. In addition, as shown in Fig. 13(a), a plethora of evanescent eigenmodes exist in the vicinity of the Dirac frequency. Fig. 16(a) reports the D3 eigenmode where a clear localised pattern can be observed, whereas Fig. 16(b)–(d) show the difference between the full and reduced Cartesian components of the eigenmodes.

Let us compare Figs. 7 and 13. The differences in accuracy between the two diagrams stem from the amount of "retained" Bloch-Floquet master nodal dofs, with respect to the full master nodes (*cf.* Figs. 3 and 5). In fact, for the 1D periodic unit cell the procedure in section 3.2 eliminates a considerable number of Bloch-Floquet master nodes, especially along the x and y directions (see Fig. 3(a) and (b)), while for the structure in Fig. 1(b) (see Fig. 5) almost all master nodal dofs are retained after the elimination procedure. Although the accuracy of Guyan eigenfrequency for free structures scales well with the amount of eliminated nodes - as demonstrated in Fig. 2 - such elimination represents a considerable source of error in calculating dispersion diagrams (see Fig. 7). The accuracy can be improved in several ways, for example including the full set of Bloch-Floquet master dofs to the reduced Guyan superelement, as presented in Fig. 8. The full/reduced comparison in Fig. 8 significantly improves with respect to that in Fig. 7. The computation time for the dispersion obtained using the Guyan superelement is approximately 1/2 than the time required to perform the full computation as only a tiny fraction (0.2%) of the total time is now required by the dynamic condensation. As expected, although the dynamic condensation is fast, the nonlinear eigenvalue problem is not sped up when keeping the full set of Bloch-Floquet master nodal dofs. In addition, we observe that the full-reduced comparison in Fig. 15(a) and (b) reports differences of order $\approx 10\%$, whereas the remaining considered eigenmodes show differences of order $\approx 1\%$. This loss in accuracy is partly due to the high-frequency considered there and partly traceable back to the fact that the dispersion diagrams in Fig. 13 have been obtained by eliminating some of the border nodes. Despite such discrepancies, the dispersive behaviour and the mode-shapes are clearly captured.

We observe that the overall performance of the dispersion calculation can be improved considering a different unit cell giving rise to the same periodic structure but comprising less Bloch-Floquet master nodes. In fact, minimizing the amount of Bloch-Floquet master nodes reduces the size of the quadratic eigenvalue problem (13), the most time consuming step in the dispersion calculation.

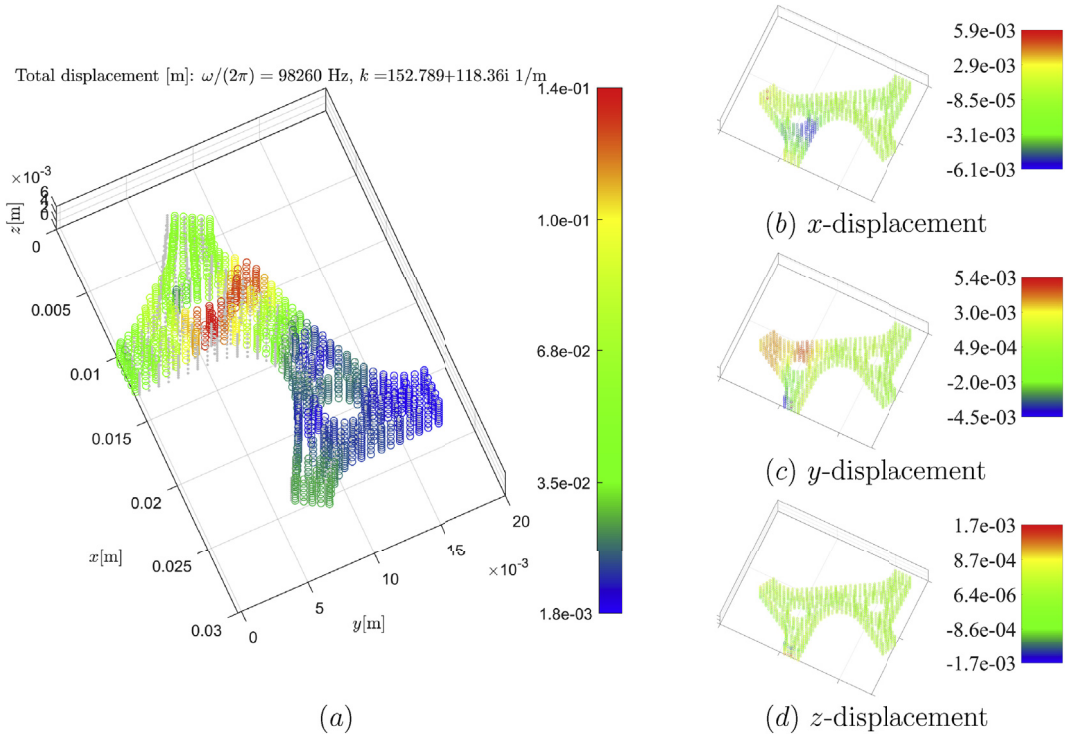

Fig. 16. Complex eigenmode corresponding to the D2 point in Fig. 13(b). The color map in panel (a) represents the norm of the eigenmode total nodal displacement (scale 10^{-2}) with respect to the non-deformed FE nodes (grey dots). Panels (b)–(d) are the difference between the full and reduced (see Eq. (32)) eigenmode (x-, y- and z-component of the displacement, respectively). The wave number corresponding to the reduced model is $k = (153.48 + 117.88i)$ [1/m]. (For interpretation of the references to color in this figure legend, the reader is referred to the Web version of this article.)

5. Conclusions

In this article, we have applied the concept of Guyan condensation to the direct Bloch-Floquet dispersion calculation in 1D and 2D periodic structures, for realistic 3D unit cells. The reduction is based on the careful elimination of nodal dofs that contribute the least to a selected set of modes of the (free) unit cell. The retained nodes are used to define a superelement, *i.e.* a reduced dynamic stiffness matrix obtained as asymptotic expansion up to $O(\omega^2)$ of the dynamically condensed equation of motion. By using the superelement, a considerable time saving is observed - down to 1/4 of the time required to perform the full calculation. The accuracy of the superelement in predicting the complex dispersion relation and associated eigenvectors, especially in the high-frequency regime, is mainly limited by the amount of nodes eliminated at the Bloch-Floquet master faces. By eliminating nodal dofs at the master Bloch-Floquet faces, one implicitly assumes that those nodes are free, while in reality they are connected to neighbouring cells. This is a delicate point as both computation time and accuracy of dispersion and eigenvectors are mainly controlled by the size of the polynomial eigenvalue problem defined over the Bloch-Floquet master dofs. If higher accuracy is required, the introduction of the full set of Bloch-Floquet master nodal dofs significantly improves the accuracy (see Fig. 8) while still allowing for a considerable reduction in computational time.

CRediT authorship contribution statement

Domenico Tallarico: Conceptualization, Methodology, Software, Formal analysis, Data curation, Visualization, Writing - original draft, Writing - review & editing. **Gwenael Hannema:** Resources, Writing - review & editing. **Marco Miniaci:** Resources, Writing - review & editing. **Andrea Bergamini:** Resources, Writing - review & editing. **Armin Zemp:** Supervision, Writing - review & editing. **Bart Van Damme:** Supervision, Project administration, Funding acquisition, Software, Methodology, Conceptualization, Writing - review & editing.

Declaration of competing interest

The authors declare that they have no known competing financial interests or personal relationships that could have appeared to influence the work reported in this paper.

Acknowledgements

The presented work is funded under an Empa Internal Research Call scheme as project number 5213.00171.100.01. The Authors gratefully acknowledge the funding that made this work possible.

References

[1] R.V. Craster, S. Guenneau (Eds.), Acoustic Metamaterials: Negative Refraction, Imaging, Lensing and Cloaking, vol. 166, Springer Science & Business Media, 2012.
[2] P. Wang, F. Casadei, S. Shang, J.C. Weaver, K. Bertoldi, Harnessing buckling to design tunable locally resonant acoustic metamaterials, Phys. Rev. Lett. 113 (2014) 014301.
[3] D. Bigoni, S. Guenneau, A.B. Movchan, M. Brun, Elastic metamaterials with inertial locally resonant structures: application to lensing and localization, Phys. Rev. B 87 (2013) 174303.
[4] D. Tallarico, N.V. Movchan, A.B. Movchan, D.J. Colquitt, Tilted resonators in a triangular elastic lattice: chirality, Bloch waves and negative refraction, J. Mech. Phys. Solid. 103 (2017) 236–256.
[5] G. Carta, I.S. Jones, N.V. Movchan, A.B. Movchan, M.J. Nieves, Deflecting elastic prism and unidirectional localisation for waves in chiral elastic systems, Sci. Rep. 7 (2017) 26.
[6] G. Carta, D.J. Colquitt, A.B. Movchan, N.V. Movchan, I.S. Jones, One-way interfacial waves in a flexural plate with chiral double resonators, Philos. Trans. R. Soc. A 378 (2019) 20190350.
[7] M. Miniaci, R.K. Pal, B. Morvan, M. Ruzzene, Experimental observation of topologically protected helical edge modes in patterned elastic plates, Phys. Rev. X 8 (2018) 031074.
[8] L. Brillouin, Wave Propagation in Periodic Structures: Electric Filters and Crystal Lattices, Dover Publications, 2003.
[9] T. Bckmann, M. Kadic, R. Schittny, M. Wegener, Mechanical cloak design by direct lattice transformation, Proc. Natl. Acad. Sci. Unit. States Am. 112 (2015) 4930–4934.
[10] A.N. Norris, A.L. Shuvalov, Elastic cloaking theory, Wave Motion 48 (2011) 525–538.
[11] M. Brun, S. Guenneau, A. Movchan, Achieving control of in-plane elastic waves, Appl. Phys. Lett. 94 (2009) 061903.
[12] D.J. Colquitt, M. Brun, M. Gei, A.B. Movchan, N.V. Movchan, I.S. Jones, Transformation elastodynamics and cloaking for flexural waves, J. Mech. Phys. Solid. 72 (2014) 131–143.
[13] A.N. Norris, Acoustic cloaking theory, Proc. R. Soc. A 464 (2008) 2411–2434.
[14] V.S. Sorokin, J.J. Thomsen, Effects of weak nonlinearity on the dispersion relation and frequency band-gaps of a periodic BernoulliEuler beam, Proc. R. Soc. A 472 (2016) 20150751.
[15] P. Packo, T. Uhl, W.J. Staszewski, M.J. Leamy, Amplitude-dependent Lamb wave dispersion in nonlinear plates, J. Acoust. Soc. Am. 140 (2016) 1319.
[16] C. Lestringant, B. Audoly, D.M. Kochmann, A discrete, geometrically exact method for simulating nonlinear, elastic and inelastic beams, Comput. Methods Appl. Mech. Eng. 361 (2019) 112741.
[17] B. Deng, Y. Zhang, Q. He, V. Tournat, P. Wang, K. Bertoldi, Propagation of elastic solitons in chains of pre-deformed beams, New J. Phys. 21 (2019) 073008.
[18] N. Nadkarni, A. Arrieta, C. Chong, D.M. Kochmann, C. Daraio, Unidirectional transition waves in bistable lattices, Phys. Rev. Lett. 116 (2016) 244501.
[19] F. Dal Corso, D. Tallarico, N.V. Movchan, A.B. Movchan, D. Bigoni, Nested Bloch waves in elastic structures with configurational forces, Phil. Trans. R. Soc. A Math. Phys. Eng. Sci. 377 (2019) 20190101.
[20] D. Tallarico, N.V. Movchan, A.B. Movchan, Scattering from a non-linear structured interface, J. Mech. Phys. Solid. 136 (2019) 103687.
[21] D.J. Mead, A general theory of harmonic wave propagation in linear periodic systems with multiple coupling, J. Sound Vib. 27 (1973) 235–260.
[22] R.S. Langley, A variational principle for periodic structures, J. Sound Vib. 135 (1989) 135–142.
[23] B. Mace, E. Manconi, Modelling wave propagation in two-dimensional structures using finite element analysis, J. Sound Vib. 318 (2008) 884–902.
[24] L. Van Belle, C. Claeys, E. Deckers, W. Desmet, On the impact of damping on the dispersion curves of a locally resonant metamaterial: modelling and experimental validation, J. Sound Vib. 409 (2017) 1–23.
[25] C. Claeys, N.G. Rocha de Melo Filho, L. Van Belle, E. Deckers, W. Desmet, Design and validation of metamaterials for multiple structural stop bands in wave guides, Extreme Mech. Lett. 12 (2017) 7–22.
[26] I.A. Veres, T. Berer, O. Matsuda, Complex band structures of two dimensional phononic crystals: analysis by the finite element method, J. Appl. Phys. 114 (2013) 083519.
[27] M. Collet, M. Ouisse, M. Ruzzene, M.N. Ichchou, Floquet-Bloch decomposition for the computation of dispersion of two-dimensional periodic, damped mechanical systems, Int. J. Solid Struct. 48 (20) (2011) 2837–2848.
[28] Y.-F. Wang, Y.-S. Wang, V. Laude, Wave propagation in two-dimensional viscoelastic metamaterials, Phys. Rev. B 92 (10) (2015) 104110.
[29] M. Mazzotti, M. Miniaci, I. Bartoli, Band structure analysis of leaky Bloch waves in 2D phononic crystal plate, Ultrasonics 72 (2017) 140–143.
[30] S.B. Platts, N.V. Movchan, R.C. McPhedran, A.B. Movchan, Two-dimensional phononic crystals and scattering of elastic waves by an array of voids, R. Soc. Lond. Proc. Ser. A Math. Phys. Eng. Sci. 458 (2026) (2002) 2327–2347.
[31] A. Aivaliotis, D. Tallarico, M.-V. d'Agostino, A. Daouadji, P. Neff, A. Madeo, Frequency- and angle-dependent scattering of a finite-sized meta-structure via the relaxed micromorphic model, Archive Appl. Mech. (2020), https://doi.org/10.1007/s00419-019-01651-9.
[32] J. Leckner, Theory of Reflection: Reflection and Transmission of Electromagnetic, Particle and Acoustic Waves, Springer, 2016.
[33] V. Laude, Y. Achaoui, S. Benchabane, K. Abdelkrim, Evanescent Bloch waves and the complex band structure of phononic crystals, Phys. Rev. B 80 (2009) 092301.
[34] P. Liu, S.X.-D. Tan, B. Yan, B. McGauchy, An extended SVD-based terminal and model order reduction algorithm, in: 2006 IEEE International Behavioral Modeling and Simulation Workshop, 2006, pp. 44–49.
[35] D.N. Herting, A general purpose, multi-stage, component modal synthesis method, Finite Elem. Anal. Des. 1 (1985) 153–164.
[36] R. Craig, M. Bampton, Coupling of substructures for dynamic analyses, AIAA J. Am. Inst. Aeronaut. Astronaut. 6 (1968) 7.
[37] R.J. Guyan, Reduction of stiffness and mass matrices, Am. Inst. Aeronaut. Astronaut. J. 3 (1965) 380.
[38] S. van Ophem, E. Deckers, W. Desmet, Efficient assembly of unit cells with Krylov based model order reduction, in: Proceedings of the International Conference on Noise and Vibration Engineering (ISMA)/International Conference on Uncertainty in Structural Dynamics (USD). KU Leuven, dept werktuigkunde, 2018, 2018.

[39] N. Bouhaddi, R. Fillod, A method for selecting master dofs in dynamic substructuring using the Guyan condensation method, Comput. Struct. 45 (1991) 941–946.
[40] A. Palermo, A. Marzani, Extended Bloch-mode synthesis: ultrafast method for the computation of complex band structures in phononic media, Int. J. Solid Struct. 100 (2016) 29–40.
[41] C. Droz, C. Zhou, M.N. Ichchou, J.-P. Lain, A hybrid wave-mode formulation for the vibro-acoustic analysis of 2D periodic structures, J. Sound Vib. 363 (2016) 285–302.
[42] R.F. Boukadia, C. Droz, M.N. Ichchou, W. Desmet, A Bloch wave reduction scheme for ultrafast band diagram and dynamic response computation in periodic structures, Finite Elem. Anal. Des. 148 (2018) 1–12.
[43] A. Bergamini, M. Miniaci, T. Delpero, D. Tallarico, B. Van Damme, G. Hannema, I. Leibacher, A. Zemp, Tacticity in chiral phononic crystals, Nat. Commun. 10 (2018) 4525.
[44] N. Bouhaddi, R. Fillod, Model reduction by a simplified variant of dynamic condensation, J. Sound Vib. 192 (2) (1996) 233–250.
[45] Z.Q. Qu, Model Order Reduction Techniques with Applications in Finite Element Analysis, Springer Science & Business Media, 2013.
[46] C.T. Leondes, Discrete-Time Control System Analysis and Design: Advances in Theory and Applications, Elsevier, 1995.